nature astronomy

ARTICLES

https://doi.org/10.1038/s41550-022-01624-z

Check for updates

High-frequency heating of the solar wind triggered by low-frequency turbulence

Jonathan Squire[1]✉, Romain Meyrand[1], Matthew W. Kunz[2,3], Lev Arzamasskiy[4], Alexander A. Schekochihin[5,6] and Eliot Quataert[2]

The fast solar wind's high speeds and non-thermal features require that considerable heating occurs well above the Sun's surface. Two leading theories seem incompatible: low-frequency 'Alfvénic' turbulence, which transports energy outwards and is observed ubiquitously by spacecraft but seems insufficient to explain the observed dominance of ion over electron heating; and high-frequency ion-cyclotron waves, which explain the non-thermal heating of ions but lack an obvious source. Here we argue that the recently proposed 'helicity barrier' effect, which limits electron heating by inhibiting the turbulent cascade of energy to the smallest scales, can unify these two paradigms. Our six-dimensional simulations show how the helicity barrier causes the large-scale energy to grow through time, generating small parallel scales and high-frequency ion-cyclotron-wave heating from low-frequency turbulence, while simultaneously explaining various other long-standing observational puzzles. The predicted causal link between plasma expansion and the ion-to-electron heating ratio suggests that the helicity barrier could contribute to key observed differences between fast and slow wind streams.

The basic mechanisms that heat the solar corona and accelerate the solar wind remain mysterious despite intensive study over many decades[1]. A successful theory must explain how energy contained in photospheric motions and magnetic fields can be liberated to cause extreme and sudden heating of the coronal plasma, along with its acceleration to velocities well in excess of the escape velocity of the Sun. Adding to the complexity, the coronal plasma is collisionless—the mean-free path of protons can be large compared with the largest observed structures—meaning that it can be far out of local thermal equilibrium. This freedom opens up a wide array of channels for plasma heating: ions might be heated more than electrons (or vice versa), or particles might gain energy preferentially in a particular direction with respect to the local magnetic field[2]. Such differences can have pronounced macroscopic consequences.

The dominant heating mechanism(s) must be consistent with an extensive array of measurements taken both remotely, from the low corona itself, and in situ, from spacecraft spread throughout the solar wind. In fast wind streams, these data indicate that the heating must be spatially extended out to several solar radii to drive observed wind speeds[3]. The mechanism must preferentially heat protons over electrons[4], while heating heavier ions (for example, α-particles) even more effectively[5]; it must heat protons in the direction perpendicular to the local magnetic field more than in the parallel direction to explain temperature anisotropies[6]; and its features and/or after-effects should be observable in the measured field fluctuations and particle distribution, particularly at the low altitudes now being explored by the Parker Solar Probe (PSP)[7].

One paradigm that can—at least in principle—satisfy the above requirements is heating through Alfvénic turbulence. Low-frequency Alfvénic motions in the low corona are observed to contain sufficient energy to power the wind[8,9], and there are well-developed theories for how such motions become turbulent following reflection from large-scale density gradients[10–12]. This turbulence transfers energy into successively smaller-scale motions perpendicular to the magnetic field (larger $k_\perp$, where $k_\perp$ is the inverse perpendicular scale), ultimately dissipating to heat the plasma. The difficulty is that most theories predict that in the strongly magnetized limit relevant to the solar corona (the low-β limit, where β is the ratio of thermal to magnetic pressure), such low-frequency, high-$k_\perp$ structures dissipate to heat predominantly electrons[13,14]. Other low-frequency plasma motions, such as compressive waves, generally cause parallel heating of ions[15]. Both possibilities are inconsistent with observations. More promisingly, for turbulence of sufficient amplitudes, 'stochastic heating'[16] can heat ions through a random walk on ion-gyroscale electric field fluctuations. Although it could plausibly explain key observations[17,18], questions remain, such as its possible quenching due to flattening of the distribution function[19,20] and the influence of cross helicity[21]. Another possibility, that ions are heated by kinetic-Alfvén-wave (KAW) turbulence at sub-gyroradius scales[19,22], remains less well understood and may be inefficient at low β (ref. [20]).

In the opposite limit of short field-parallel wavelengths (large $k_\parallel$), high-frequency ion-cyclotron waves (ICWs) provide a simpler mechanism for strong perpendicular ion heating[6,23]. At wavenumbers approaching $k_\parallel \approx d_i^{-1}$, where d_i is the ion inertial length, their frequency approaches the ion gyrofrequency, where the cyclotron resonance causes highly efficient energy transfer from electromagnetic fields to ion velocities[24,25]. ICWs are observed ubiquitously in situ[7] and can suprathermally heat minor ions in a way that is observationally compelling[26,27]. However, a sufficiently energetic direct solar source of ICWs is highly unlikely[28], and the Alfvénic cascade does not efficiently transfer energy to small parallel scales[29], seemingly ruling out their turbulent origin. Although their occurrence in data can be explained by kinetic instabilities[30], in most theories this implies that they would cool, rather than heat, the plasma[24]; except perhaps in the presence of strong non-thermal particle beams[31].

[1]Physics Department, University of Otago, Dunedin, New Zealand. [2]Department of Astrophysical Sciences, Princeton University, Princeton, NJ, USA. [3]Princeton Plasma Physics Laboratory, Princeton, NJ, USA. [4]School of Natural Sciences, Institute for Advanced Study, Princeton, NJ, USA. [5]The Rudolf Peierls Centre for Theoretical Physics, University of Oxford, Clarendon Laboratory, Oxford, UK. [6]Merton College, Oxford, UK. ✉e-mail: jonathan.squire@otago.ac.nz

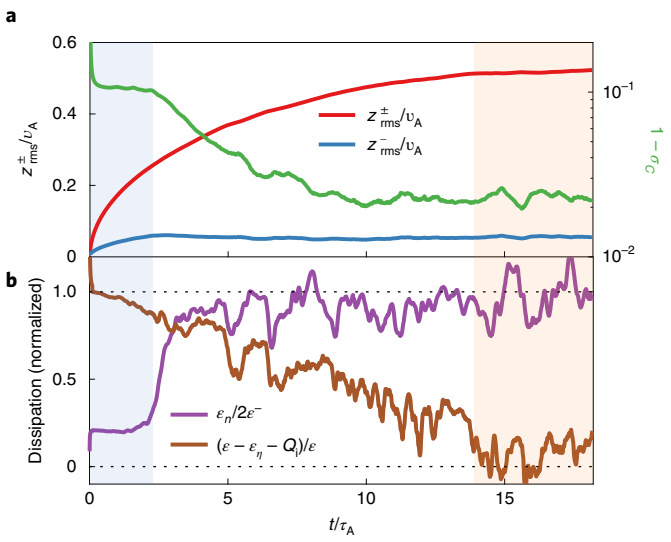

Fig. 1 | The time evolution confirms the formation of the helicity barrier. **a**, Outward-/inward-propagating fluctuation amplitudes (left *y* axis) and imbalance (right *y* axis). **b**, Energy budget and heating, illustrated through the ion heating rate (Q_i) and the small-scale resistive dissipation (ε_η). The balanced part of the injected energy (~$2\varepsilon^-$) saturates early by $t \simeq 3\tau_A = 3L_{||}/v_A$ (blue shaded region); this is demonstrated by the saturation of z^- (blue line in **a**) and the resistive dissipation (purple line in **b**), which absorbs only a small fraction of the input energy $\varepsilon_\eta \approx 2\varepsilon^- \ll \varepsilon$. Eventually, by $t \approx 14\tau_A$ (orange shaded region), ion heating absorbs the remainder of the injected energy so that $Q_i \approx \varepsilon - \varepsilon_\eta$ (brown line in **b**), halting the growth of z^+. A numerical cooling effect has been removed to compute the energy budget (Methods and Extended Data Fig. 1).

If combined, these two heating paradigms—via Alfvénic turbulence or ICWs—can conceivably satisfy the fast-wind heating requirements described above, maintaining an abundant source of perpendicular ion heating well above the solar surface. Here we assess whether a newly discovered effect, termed the helicity barrier[32], can fulfil this role by obstructing the dissipation of collisionless Alfvénic turbulence into electron heat. Using six-dimensional, high-resolution, hybrid-kinetic simulations, we explore the effect of the helicity barrier on collisionless turbulent heating, choosing parameters to match the conditions observed in fast wind streams as closely as possible. We assess the relevance of our results to the solar wind by comparing detailed features of the turbulent spectra and ion distribution function to observations from PSP and other spacecraft.

The helicity barrier

Solar-wind turbulence is imbalanced (possessing cross helicity), meaning that it is energetically dominated by Alfvénic structures that propagate outwards from the Sun (designated z^+; the inward-propagating component is designated z^-). The theory of highly perpendicular ($k_\perp \gg k_{||}$) perturbations in a collisionless plasma predicts that, at scales larger than the ion gyroradius ρ_i, imbalanced turbulent Alfvénic energy in $z^\pm$ can cascade towards smaller scales (larger $k_\perp$), as required to heat the plasma[15]. In contrast, at sub-gyroradius scales $k_\perp\rho_i \gtrsim 1$, magnetic helicity conservation implies the opposite: imbalanced energy must cascade inversely, towards larger scales[15,32,33]. The effect is directly analogous to two-dimensional hydrodynamic turbulence, where enstrophy conservation causes energy to cascade inversely, creating large-scale vortex structures. However, unlike in hydrodynamics, in low-β plasmas, cross helicity at $k_\perp\rho_i \lesssim 1$ transforms conservatively into magnetic helicity at $k_\perp\rho_i \gtrsim 1$ (the system conserves a generalized helicity[32]). This implies that an imbalanced energy flux arriving at $k_\perp\rho_i \approx 1$ from large scales cannot cascade to arbitrarily small scales.

Mathematically, it is helpful to separate the turbulent energy flux ε into components associated with the large-scale outward (ε^+) and inward (ε^-) propagating fluctuations: $\varepsilon = \varepsilon^+ + \varepsilon^-$. Generalized helicity conservation prohibits the conversion of ε^+ into ε^- at any scale (note, however, that at $k_\perp\rho_i \gtrsim 1$, ε^+ is associated with a mixture of outward- and inward-propagating KAWs). Because a forward cascade must be balanced ($\varepsilon^+ \approx \varepsilon^-$) at $k_\perp\rho_i \gtrsim 1$, only a small portion ~$2\varepsilon^-$ of the energy flux can cascade to the small scales at which it will heat electrons[14]. The rest of the flux, ~$(\varepsilon^+ - \varepsilon^-)$, is stuck—it hits the helicity barrier and thus remains at scales $k_\perp\rho_i \lesssim 1$. If the system is forced continuously, this large-scale energy grows in time with a decreasing parallel correlation length[32], as expected from critical balance[15]. We show that this growth eventually funnels the turbulent energy into a spectrum of ICW fluctuations, heating the ions, which absorb the majority of the energy flux.

Numerical method

Our simulation used the PEGASUS++ code[34], which solves the hybrid-kinetic equations with isothermal electrons using the particle-in-cell method. The system was strongly magnetized with mean magnetic field $\mathbf{B}_0 = -B_0\hat{\mathbf{z}}$, Alfvén speed $v_A = B_0/\sqrt{4\pi n m_i}$ and initial ion β, $\beta_i \equiv 8\pi n k_B T_i/B_0^2 = 0.3$ (where m_i, n and $k_B T_i = m_i v_{th}^2/2$ are the ion mass, number density and temperature, respectively, with v_{th} the ion thermal velocity and k_B the Boltzmann constant). Perpendicular (*x*- and *y*-directed) ion-velocity fluctuations $\mathbf{u}_\perp$ and magnetic fluctuations $\mathbf{B}_\perp$ were driven at large scales and correlated to create imbalance, with $\mathbf{z}^+ \equiv \mathbf{u}_\perp + \mathbf{B}_\perp/\sqrt{4\pi n m_i} \gg \mathbf{z}^- \equiv \mathbf{u}_\perp - \mathbf{B}_\perp/\sqrt{4\pi n m_i}$ ($\mathbf{z}^+$ perturbations propagate in the $+\hat{\mathbf{z}}$ direction). The energy-injection rate ε and cross-helicity injection rate $\varepsilon_H = \varepsilon^+ - \varepsilon^- = 0.9\varepsilon$ were constant in time. Plasma heating was strongly influenced by the amplitude $\delta B_\perp/B_0$ and spectral anisotropy $k_{||}/k_\perp$ of fluctuations with $k_\perp\rho_i \approx 1$. To reach realistic values without simulating the enormous scale separation of the real solar wind, we used a highly elongated box with dimensions $L_{||} = L_z = 6L_\perp$; given the box size $k_{\perp 0}\rho_i \equiv 2\pi\rho_i/L_\perp \approx 0.05$, this gave conditions near $k_\perp\rho_i \approx 1$ that were comparable to those observed[35]. The elongated domain also implies that the timescales we probed were rapid compared with the solar wind's outer scales and its expansion rate, justifying the external forcing to represent a turbulent flux from larger scales[36] and our neglect of expansion effects. The simulation's resolution was $N_\perp^2 \times N_{||} = 392^2 \times 2{,}352$ cells, so that the smallest resolved scales had $k_{\perp,\max}\rho_i \simeq \pi N_\perp \rho_i/L_\perp = 10$. Most other simulation parameters, including a (hyper-)resistivity η_4 that dissipated small-scale magnetic energy, were chosen to match a previous balanced turbulence simulation with $\beta_i = 0.3$ (ref. [19]). This allowed direct comparison with their spectra and heating. Further details are provided in Methods.

Results

The simulation's evolution through time, shown in Fig. 1, exhibits several features that are expected from the helicity barrier[32] but not from other theories of imbalanced turbulence[32,37]. Figure 1a shows the growth of the root-mean-square amplitudes $z^\pm_{rms}/v_A \equiv \langle (z^\pm)^2 \rangle^{1/2}/v_A$ and imbalance (normalized cross helicity) $\sigma_c = 2\langle \sqrt{4\pi n m_i}\mathbf{u}\cdot\mathbf{B} \rangle / \langle 4\pi n m_i \mathbf{u}^2 + \mathbf{B}^2 \rangle$ (where $\langle \dots \rangle$ denotes a box average). Because $z^+_{rms}/v_A \approx 2u_{\perp,rms}/v_A \approx 2B_{\perp,rms}/B_0$, the final $\delta B_\perp/B_0 \approx 0.26$ was nearly twice that of the balanced simulation ($\delta B_\perp/B_0 \approx 0.14$). We see that z^- saturates quickly, by time $t \simeq 3\tau_A$, whereas saturation of z^+ occurs only after $t \simeq 14\tau_A$ ($\tau_A \equiv L_{||}/v_A$ is the Alfvén time). This is expected: energy in z^- can cascade to $k_\perp\rho_i \gtrsim 1$ through standard KAW turbulence, whereas most of the energy in z^+ cannot cascade past $k_\perp\rho_i \approx 1$ due to the helicity barrier. The imbalance saturates at $\sigma_c \approx 0.98$, which, although large, is regularly observed by PSP[38]. Figure 1b shows the ion heating rate

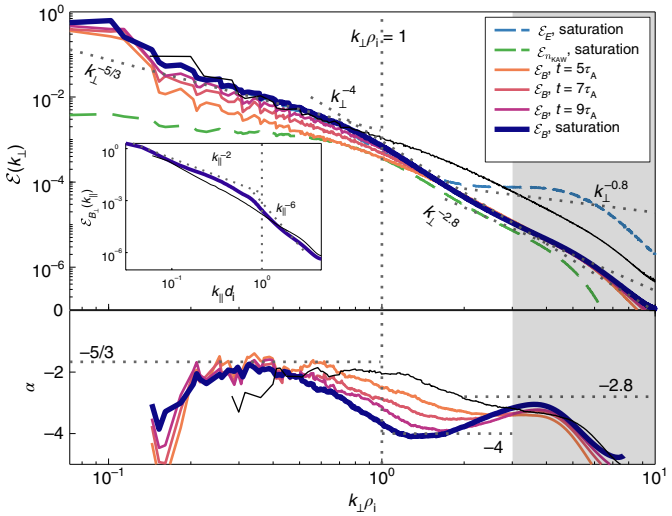

Fig. 2 | Fluctuation spectra exhibit a steep transition region around $k_\perp\rho_i = 1$. Top: spectra of the magnetic field $\mathcal{E}_\mathbf{B} = \mathcal{E}_{B_x} + \mathcal{E}_{B_y} + \mathcal{E}_{B_z}$, electric field $\mathcal{E}_\mathbf{E} = \mathcal{E}_{E_x} + \mathcal{E}_{E_y} + \mathcal{E}_{E_z}$ and KAW-normalized density $n_{KAW} = \sqrt{\beta_i(1+2\beta_i)}n$, binned in $k_\perp = \sqrt{k_x^2 + k_y^2}$. The inset shows the extremely steep $k_\parallel$ spectrum of $B_\perp$ ($\mathcal{E}_{B_\perp} = \mathcal{E}_{B_x}\mathcal{E}_{B_y}$) near $k_\parallel d_i = 1$. Bottom: local scaling exponents, $\alpha = \mathrm{d}\ln\mathcal{E}/\mathrm{d}\ln k_\perp$; at small scales (approximately the grey shaded region) spectra are affected by particle noise (Extended Data Fig. 2). Thin black lines show $\mathcal{E}_\mathbf{B}$ for an analogous balanced-turbulence simulation[19].

$Q_i = V\partial_t\langle 3m_i v_{th}^2/2\rangle$ (where V is the simulation volume) and the hyper-resistive dissipation rate ε_η. The latter is a proxy for electron heating because it absorbs the energy that cascades to the smallest scales below where ions cannot respond to the fluctuations. We see that ε_η saturates rapidly, together with z^- and well before the total energy. Its value, $\varepsilon_\eta \approx 2\varepsilon^-$, approximates the balanced portion of the injected flux, as expected. The remainder of the energy input, $\varepsilon - \varepsilon_\eta$, must eventually go into Q_i. However, for this to happen, z^+ must grow considerably; notably, this occurs without change to ε_η or z^-. The simulation saturates with $Q_i \approx \varepsilon - \varepsilon_\eta$ at $t \approx 14\tau_A$; we ran it for another $t \approx 4.2\tau_A$ in this steady state.

Perpendicular magnetic ($\mathcal{E}_\mathbf{B}$), electric ($\mathcal{E}_\mathbf{E}$), and density ($\mathcal{E}_{n_{KAW}}$) fluctuation spectra are shown in Fig. 2. The signature of the helicity barrier is the sharp spectral break at $k_\perp\rho_i < 1$ in $\mathcal{E}_\mathbf{B}$ and $\mathcal{E}_\mathbf{E}$, which migrates to larger scales with time[32]. 'Double-kinked' spectra—an $\sim k_\perp^{-5/3}$ range at large scales, a steep $\sim k_\perp^{-4}$ transition range bracketing $k_\perp\rho_i = 1$ and a flatter range of KAW turbulence ($\sim k_\perp^{-2.8}$) at yet smaller scales—have been observed for decades[39] including by PSP close to the Sun[40], but have lacked a clear theoretical explanation and have not been previously observed in simulations. Although $\mathcal{E}_\mathbf{B}$ in Fig. 2 lacks an $\sim k_\perp^{-2.8}$ range due to box resolution (resistivity), it clearly reflattens at $k_\perp\rho_i \approx 2$, and the width of the transition range is comparable to observations[40]. The $\mathcal{E}_\mathbf{E}$ spectrum has a similar shape, flattening after a steep drop around $k_\perp\rho_i \approx 1$. The spectrum of $n_{KAW} = \sqrt{\beta_i(1+2\beta_i)}n$ was predicted[15] and observed[41] to satisfy $\mathcal{E}_{n_{KAW}} \approx \mathcal{E}_\mathbf{B}$ in KAW turbulence because linear KAWs satisfy $\delta B_\perp/B_0 \approx (\delta n/n)\sqrt{\beta_i(1+\beta_i)} \approx (\delta B_\parallel/B_0)\sqrt{1+1/\beta_i}$ and $\delta B^2 = \delta B_\perp^2 + \delta B_\parallel^2$; this occurs here for $k_\perp\rho_i \gtrsim 1$, providing further evidence for the KAW-like nature of the sub-ρ_i turbulence. The parallel spectrum (see the inset in the top panel of Fig. 2 and Methods) exhibits an $\sim k_\parallel^{-2}$ range at large scales, followed by a very steep $\sim k_\parallel^{-6}$ range bracketing $k_\parallel d_i \approx 1$, which flattens at smaller scales; again these features match recent PSP observations[42]. Balanced turbulence[19], unlike the imbalanced case, does not exhibit a steep transition range in either $k_\perp$ or $k_\parallel$, which is probably also the case in the solar wind[43]. Note that spectra are adversely affected by particle noise for $k_\perp\rho_i \gtrsim 3$ (Methods and Extended Data Figs. 1 and 2).

Evidence for the presence of ICWs in the saturated state is shown in Fig. 3. The projected magnetic field lines and electric field (Fig. 3a) reveal the coexistence of $k_\parallel d_i \approx 1$ parallel structure with the sub-ρ_i striations of KAW turbulence in the perpendicular plane. More quantitatively, Fig. 3b shows the two-dimensional $(k_\perp, k_\parallel)$ spectrum of $B_\perp$ (Methods and Extended Data Fig. 3). Several features are manifest: first, unlike in the analogous balanced-turbulence simulation[19], the outer-scale parallel correlation length is markedly smaller than $L_\parallel$ because it decreases with increasing amplitude to maintain critical balance, $k_\parallel v_A \approx k_\perp z^+$ (the region of maximal spectral power moves upwards in time as z^+ grows); second, the cone of maximal spectral power seems to steepen as the turbulence moves to smaller scales, creating small parallel scales faster than the canonical result[15] $k_\parallel \propto k_\perp^{2/3}$ (or $k_\parallel \propto k_\perp^{1/2}$ for aligned turbulence[37]); third, there is a clear spectral bump at $k_\parallel d_i \simeq 0.8$ and $k_\perp < k_\parallel$, the signature of ICWs. By integrating the energy spectrum over modes with $k_\perp \leq k_\parallel$, we estimated that these ICW modes contain ≃1% of the total energy; this fraction grows by a factor of ≃50 from $t \simeq 5\tau_A$ to saturation and exceeds that of saturated balanced turbulence by a factor of ≃30. We confirm that these modes are in fact ICWs in Fig. 3c, which shows the normalized magnetic-helicity spectrum $k\mathcal{H}_\mathbf{k}/\mathcal{E}_\mathbf{B}$, where $\mathcal{H}_\mathbf{k} = \mathrm{i}(B_x^* B_y - B_y^* B_x)/k_z$, binned in $(k_\perp, k_z)$. As predicted[44] and observed[45], ICWs (with $k_\perp \lesssim k_\parallel$) are characterized by $k\mathcal{H}_\mathbf{k}/\mathcal{E}_\mathbf{B} < 0$, whereas $k\mathcal{H}_\mathbf{k}/\mathcal{E}_\mathbf{B} > 0$ for $k_\perp \gtrsim k_\parallel$ near $k_\perp\rho_i \simeq 1$. This results from the intrinsic polarization of ICWs and their propagation direction; $k\mathcal{H}_\mathbf{k}/\mathcal{E}_\mathbf{B} \approx -1$ indicates that ICWs propagate almost exclusively in the $+\hat{\boldsymbol{z}}$ direction, like the large-scale z^+. At $k_\perp > k_\parallel$, $k\mathcal{H}_\mathbf{k}/\mathcal{E}_\mathbf{B} > 0$ is a result of the dominantly Alfvénic perturbations becoming dispersive at $k_\perp\rho_i \approx 1$; helicity grows to $k\mathcal{H}_\mathbf{k}/\mathcal{E}_\mathbf{B} \approx 0.5$ at $k_\perp\rho_i \simeq 1$ before decreasing again because the small-scale KAW cascade is balanced. This feature, which is a theoretical corollary of the helicity barrier, has been commonly observed by PSP and other spacecraft[45] and correlates with the transition-range spectral slope as predicted[46].

Evidence that plasma heating occurs through ICWs is provided in Fig. 4. Quasilinear cyclotron-heating theory[24] is based on the idea that ions and ICWs interact strongly if the wave frequency $\omega_\mathbf{k}$ is resonant with the Doppler-shifted ion gyromotion. When ICWs exist across a range of $k_\parallel$, the process flattens the ion distribution function $f_i(w_\perp, w_\parallel)$ along specific 'scattering contours', which can be computed[25] from $\omega_\mathbf{k}$ for waves of a particular $k_\perp$ ($w_\perp$ and $w_\parallel$ are the field-perpendicular and field-parallel velocities of ions in the frame moving with the plasma). Theory suggests that, because the scattering contours steepen with increasing $k_\perp/k_\parallel$, heating by oblique ICWs generates an f_i that increases along the scattering contours of parallel ICWs[47]. The consequences are twofold: first, oblique-ICW heating generates parallel ICWs, explaining the dominance of $k_\perp \ll k_\parallel$ modes in Fig. 3b; second, in a quasi-steady state, f_i is nearly flat along the parallel ICW scattering contours. We plot these, along with $f_i(w_\perp, w_\parallel)$, in Fig. 4a. There is exceptionally good agreement at saturation for $w_\parallel \lesssim -w_{\parallel,d_i}$ particles, which are those that can resonate with $k_\parallel d_i \lesssim 1$ ICWs propagating in the $+\hat{\boldsymbol{z}}$ direction (Methods). The time evolution is also telling: the quasilinear flattening starts at large $|w_\parallel|$ and moves upwards as time advances, which is expected because there is more power in low-$k_\parallel$ modes that resonate with high-$|w_\parallel|$ ions. Figure 4b shows the perpendicular energy diffusion coefficient $D^E_{\perp\perp}$, computed for $w_\parallel < -w_{\parallel,d_i}$ using the time evolution of f_i (ref. [48]) and validated by computing $\langle \mathbf{E}_\perp \cdot \mathbf{w}_\perp \rangle$ directly from particle trajectories[20]. Quasilinear ICW theory predicts[24] that $D^E_{\perp\perp} \propto w_\perp^2$, as seen in Fig. 4, whereas a stochastically heated plasma has approximately constant[20] $D^E_{\perp\perp}$ for $w_\perp \sim v_{th}$. This quantitatively confirms the dominance of quasilinear ICW heating and we find no other evidence for stochastic heating in this simulation, although

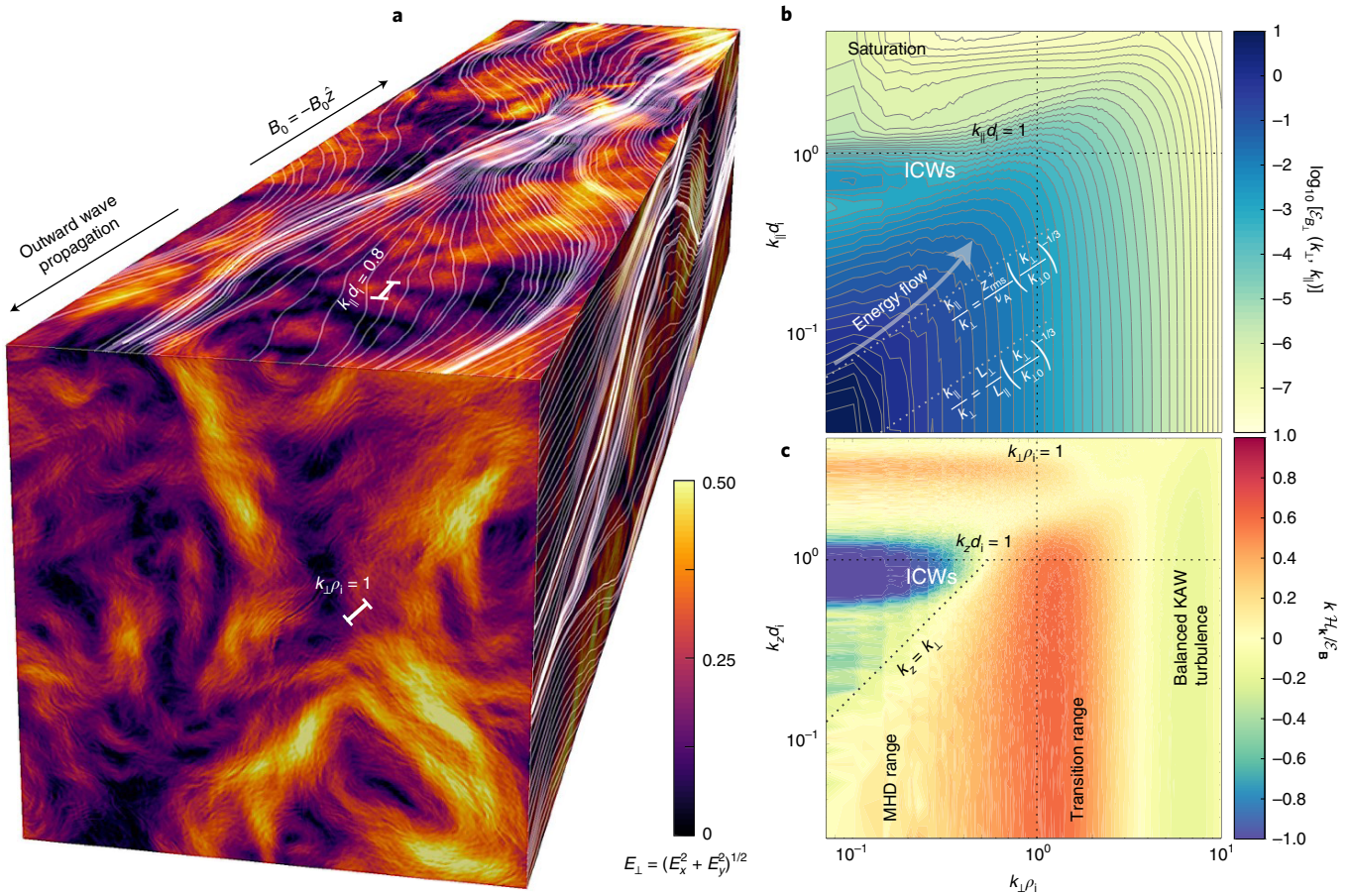

Fig. 3 | Evidence for ICW fluctuations in the saturated state. a, Structure of $E_\perp$. The superimposed white lines show magnetic field lines projected onto the plane. **b**, Perpendicular magnetic-field fluctuation spectrum ($\mathcal{E}_{B_\perp} = \mathcal{E}_{B_x} + \mathcal{E}_{B_y}$) in ($k_\perp, k_\parallel$), shown with a logarithmically spaced colour bar and contours; this illustrates the path of energy to $k_\parallel d_i \simeq 1$ scales (labelled 'energy flow') and the parallel ICW bump at $k_\parallel d_i \simeq 0.8$. The white dotted lines show the canonical critical balance result[15] based on $z^+_{\rm rms}$ (top) or the outer scale of the box (bottom), and the black dotted lines indicate $k_\perp \rho_i = 1$ and $k_\parallel d_i = 1$. **c**, $k\mathcal{H}_\mathbf{k}/\mathcal{E}_\mathbf{B}$ in ($k_\perp, k_z$), showing the reversed helicity signatures of KAWs ($k_\perp \gg k_\parallel$) and ICWs ($k_\parallel \gg k_\perp$). For perpendicular structures, $\mathcal{H}_\mathbf{k} \approx 0$ at both large scales $k_\perp \rho_i \ll 1$ (because large-scale Alfvén waves are non-helical) and in the KAW range $k_\perp \rho_i \gg 1$ (because the KAW turbulence must be balanced). In the transition range around $k_\perp \rho_i \simeq 1$, $k\mathcal{H}_\mathbf{k}/\mathcal{E}_\mathbf{B}$ has a local maximum because the Alfvénic fluctuations are both dispersive and imbalanced.

it is possible that it could govern saturation under different conditions (for example, lower β; Methods and Extended Data Fig. 4). Finally, we see a clear flattening of $f_i(w_\perp, w_\parallel)$ at $w_\parallel \approx v_A$ and small $w_\perp$, which forms a modestly super-Alfvénic beam feature in the direction of dominant wave propagation, similar to those observed in the fast solar wind[2,49,50]. By comparing $\partial f_i/\partial t$ with $\langle E_\parallel w_\parallel \rangle$ (Extended Data Fig. 5), we confirm that this arises through Landau damping of Alfvén waves as their phase velocity increases near $k_\perp \rho_i \approx 1$(ref. [51]).

Discussion

Together, Figs. 3 and 4 provide strong evidence for heating through ICWs generated by imbalanced Alfvénic turbulence regulated by the helicity barrier. Given the excellent match with in situ observations of spectra, helicity and distribution functions, we suggest that the same is true in the fast solar wind, reconciling the paradigms of low-frequency Alfvénic turbulence and ICW heating. If, as suggested above, ICWs are produced by the decrease in outer parallel scale with increasing amplitude, then the turbulence will saturate once it has grown sufficiently for $k_\parallel d_i \approx 1$ scales to be reached (where Alfvén waves become ICWs) before the $k_\perp \rho_i \approx 1$ scales (where Alfvén waves become KAWs). If large-scale fluctuations are critically balanced with spectrum $\mathcal{E}_\mathbf{B} \propto k_\perp^{-5/3}$, this suggests a critical outer-scale ($\sim L_\perp$) saturation amplitude for appreciable ICW heating given by $\delta z^+/v_A \approx A\beta_i^{1/2}(\rho_i/L_\perp)^{-1/3}$, with our simulation giving a proportionality factor $A \simeq 0.2$ (an observationally testable prediction). A corollary is that the energy-injection rate sets only the timescale to reach saturation and not the amplitude, unlike standard viscous damping. Correspondingly—and in contrast to other possible ion-heating mechanisms—if the amplitude of the fluctuations is too small at some time (or in some region of a radially stratified wind), then energy is not deposited into electrons. Instead, the helicity barrier halts the cascade, storing the energy in fluctuations that keep growing, to eventually heat ions through ICWs. This mechanism is expected to become more robust with decreasing β, at least for $\beta \gg m_e/m_i$ (for $\beta \approx m_e/m_i$, electron heating effects are important at $k_\perp \rho_i \approx 1$). Our finding that the helicity barrier occurs even at modest β ($\beta \approx 0.3$) indicates that it should apply nearly everywhere in the corona. Thus, the ratio of electron to ion heating—an important input to larger-scale models of the solar wind and other astrophysical objects—is simply $Q_i/Q_e \approx \varepsilon_H/(\varepsilon - \varepsilon_H)$ for saturated imbalanced Alfvénic turbulence, nearly independent of β for $m_e/m_i \ll \beta \lesssim 1$.

A heating ratio that is controlled by imbalance is appealing to explain the generation of fast and slow wind streams by reflection-driven Alfvénic turbulence. Fast wind—which emerges from coronal holes with lower expansion factors[52] and thus less wave reflection and larger $\varepsilon_H/\varepsilon$—is observed to have hotter protons, strong minor-ion heating, cooler electrons, larger imbalance and steep transition-range spectra. Slow wind—which arises from less

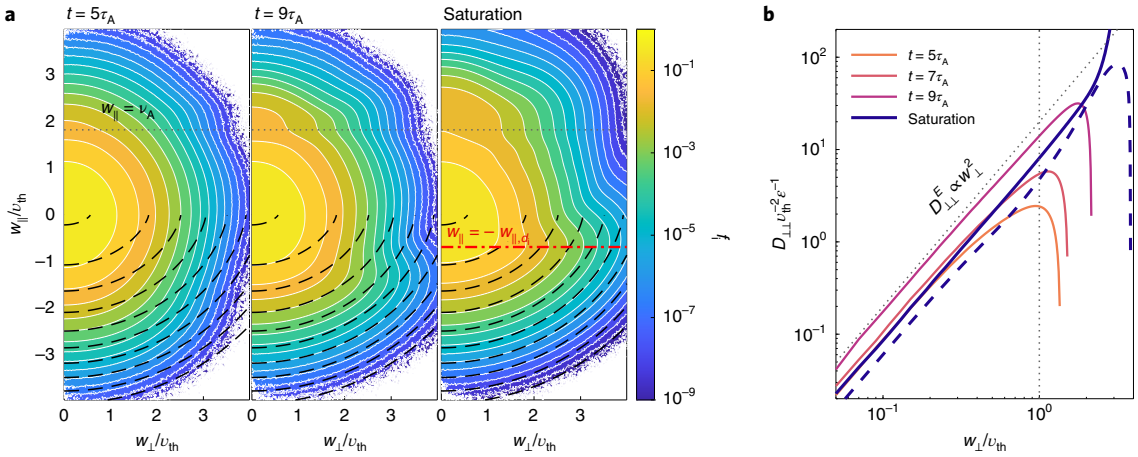

Fig. 4 | The evolution of the ion distribution function $f_i(w_\perp, w_\parallel)$ shows how ICWs heat ions. a, Structure of f_i at the times indicated, shown with a logarithmically spaced colour bar and contours. At saturation (right), f_i aligns nearly perfectly with the scattering contours of parallel ICWs (dashed lines) for $w_\parallel \lesssim -w_{\parallel,d_i}$ (red line), which is the region of velocity space where resonant ICWs exist. **b**, Perpendicular energy diffusion coefficient. Solid lines include only $w_\parallel < -w_{\parallel,d_i}$; the dashed line includes all $w_\parallel$, with the lower values of $D^E_{\perp\perp}$ indicating less heating for $w_\parallel > 0$.

ordered fields involving closed loops and/or larger expansion factors, and thus has smaller $\varepsilon_H/\varepsilon$, or even $\varepsilon_H/\varepsilon \ll 1$ in a closed-field region—is observed to have cooler protons, little suprathermal minor-ion heating, hotter electrons and less imbalance, and does not usually exhibit a steep kinetic transition range. Although reflection-driven turbulence models can already reproduce the observed correlation of expansion factor with wind speed based on the radial location of energy deposition[53,54], the additional physics afforded by the helicity barrier yields interesting implications. First, it would naturally explain the other aforementioned correlations of electron and ion thermodynamics with wind speed. Second, because of the high thermal speeds of electrons, a given quantity of energy deposited into ion heat generally drives a higher asymptotic wind velocity than if electrons are heated[4]. We propose that the helicity barrier could act as a 'switch' effect, supplementing other turbulent heating physics: low-expansion regions with a robust barrier would heat predominantly ions at large radii, ideal conditions for generating fast wind speeds; high-expansion regions would break the barrier, depositing energy into electron heat and exacerbating the inefficient acceleration that results from heating at lower radii. Thus, by linking plasma thermodynamics to magnetic-field expansion, it is plausible that the helicity barrier plays an important role in generating the bimodal speed distribution of the solar wind.

Methods

Hybrid-kinetic simulation method. The equations of the hybrid-kinetic model solved by PEGASUS++ are[34,55]:

$$\frac{\partial f_i}{\partial t} + \mathbf{v}\cdot\nabla f_i + \left[\frac{e}{m_i}\left(\mathbf{E} + \frac{\mathbf{v}}{c}\times\mathbf{B}\right) + \frac{\mathbf{F}^U_\perp}{m_i}\right]\cdot\frac{\partial f_i}{\partial \mathbf{v}} = 0, \quad (1)$$

$$\frac{\partial \mathbf{B}}{\partial t} = -c\nabla\times(\mathbf{E} + \mathbf{F}^B_\perp) + \eta_4\nabla^4\mathbf{B}, \quad (2)$$

$$\mathbf{E} = -\frac{\boldsymbol{u}_i\times\mathbf{B}}{c} + \frac{(\nabla\times\mathbf{B})\times\mathbf{B}}{4\pi e n_i} - \frac{T_e\nabla n_i}{e n_i}. \quad (3)$$

The kinetic equation (1) is solved in a six-dimensional $(\mathbf{x}, \mathbf{v})$ space using a particle-in-cell method, while Faraday's law equation (2) and the kinetic Ohm's law equation (3) are solved on a three-dimensional grid. A single ion species of charge e and mass m_i is assumed, c is the speed of light, and $\mathbf{F}^U_\perp$ and $\mathbf{F}^B_\perp$ are the forcing terms, described below. In equation (3), $n_i = \int d\mathbf{v} f_i$ and $\boldsymbol{u}_i = n_i^{-1}\int d\mathbf{v}\,\mathbf{v} f_i$ are computed from f_i. Equations (1)–(3) are derived from the two-species Vlasov equation by expanding the electron equation in $m_e/m_i \ll 1$, assuming quasi-neutrality $n_e = n_i = n$ and isothermal electrons (temperature T_e). PEGASUS++ uses a second-order accurate predictor–predictor–corrector scheme to enforce the kinetic Ohm's law[34] and has been highly optimized for efficient operation on large supercomputing systems. The hyper-resistivity in equation (2) is not intended to represent a true physical resistivity (it does not contribute to the electric field in the particle push), but is included to dissipate energy in the magnetic field at the smallest grid scales. This is a proxy for electron heating in the model.

Simulation parameters. As discussed in the main text, the simulation domain is elongated by a factor of 6 ($L_x = L_y = 67.5d_i$ and $L_z = 404.7d_i$, but with cubic grid cells $N_x = N_y = 392$, $N_z = 2{,}352$) to realize realistic solar-wind conditions near $k_\perp\rho_i \approx 1$. These conditions can be estimated roughly by taking the outer-scale fluctuations to be in approximate critical balance $\delta B_\perp/B_0 \simeq L_\perp/L_\parallel$, and assuming a magnetic spectrum $\mathcal{E}_B(k_\perp) \propto k_\perp^{-5/3}$ and $k_\parallel \propto k_\perp^{2/3}$ in the magnetohydrodynamic (MHD) inertial range[15,56]. Given the outer perpendicular scale $k_{\perp 0}\rho_i \equiv 2\pi\rho_i/L_\perp \approx 0.05$, this suggests that at $k_\perp\rho_i \approx 1$ the spectral anisotropy is $k_\perp/k_\parallel \simeq \tan 86.5°$ with fluctuation amplitude $\delta B_\perp/B_0 \simeq 0.06$. This is comparable to observed values (in fact, it is somewhat more anisotropic than many measurements; see fig. 1 in ref. [35]), justifying the appropriateness of our study to solar wind heating. We also note that the elongated simulation domain implies that the inferred outer scale (the scale at which $\delta B_\perp \approx B_0$) has an extremely long turnover time $\simeq (L_\parallel/L_\perp)^2\tau_A$ (where $\tau_A = L_\parallel/v_A$), which is also comparable to the heating time $\tau_{heat} \approx (3/2m_i)T_i V/\varepsilon$ (where $V = L_\perp^2 L_\parallel$ is the volume). Because these outer-scale timescales exceed the duration of the simulation ($\simeq 18\tau_A$), it is apt to consider the outer-scale forcing in our simulation as representing a turbulent flux of energy arriving from larger scales, even if the outer scales are decaying[36] (as relevant to the solar wind). Similarly, we note that the direct effect of solar-wind expansion is negligible at these scales. A simple estimate can be obtained by matching the simulation's ion-inertial scale to that in the solar wind, defining the expansion time as $\tau_{exp} \approx R/U$, where R is the heliocentric radius and U is the bulk solar-wind velocity. Using parameters similar to PSP's first perihelion[7,57], which also had $\beta_i \approx 0.3$, yielded $\tau_A/\tau_{exp} \simeq 8\times10^{-4}(U/350\,\mathrm{km\,s^{-1}})(R/35R_\odot)^{-1}(B/80\,\mathrm{nT})^{-1}$, illustrating that the expansion of the box is negligible ($\simeq 1.5\%$) over the simulation's duration.

Other parameters of the imbalanced simulation were chosen to match the balanced turbulence simulation of ref. [19], which had a resolution of $N_\perp^2 \times N_\parallel = 200^2 \times 1{,}200$, a smaller box with $k_{\perp 0}\rho_i \equiv 2\pi\rho_i/L_\perp \approx 0.1$ and saturated amplitude $\delta B_\perp/B_0 \approx 0.14 \simeq L_\perp/L_\parallel = 1/6$. The energy-injection rate was computed from $\varepsilon/V = C_A\delta u_{\perp 0}^2/\tau_A$, with $\delta u_{\perp 0}/v_A = L_\perp/L_\parallel$ and a Kolmogorov constant $C_A = 0.29$ to match that measured from the balanced simulation. This implies lower energy injection per unit volume in the imbalanced case, compensating for the slower outer-scale motions in its larger box; stated differently, with this C_A, turbulence in the larger $k_{\perp 0}\rho_i \approx 0.05$ box would saturate with $\delta B_\perp/B_0 \approx 0.14$ if the forcing were balanced, which also implies that it would have a smaller amplitude (smaller $k_\parallel/k_\perp$) at $k_\perp\rho_i \approx 1$. The simulation was initialized by randomly drawing particle velocities from a stationary Maxwellian distribution with temperature $T_i = T_e$. We used $N_{ppc} = 216$ particles per cell and the full-f method[34], with particles initially evenly distributed within the cell. In computing the gridded moments of f_i, we used two filter passes to reduce the impact of the particle noise[34].

The value of the hyper-resistivity, $\eta_4 \approx 2.4\times10^{-5}d_i^4\Omega_i$, was also chosen to match that of the balanced simulation (here Ω_i is the ion gyrofrequency). Its value is not intended to represent reality, but just to absorb magnetic energy that cascades to the grid scales of the simulation. We have tested the impact of this

choice by restarting the simulation in the saturated regime (at $t \simeq 16.3\tau_A$) with $\eta_4 \approx 1.6 \times 10^{-5} d_i^4 \Omega_i$. This modification extends $\mathcal{E}_{B\perp}(k_\perp)$ to smaller scales where it flattens further, as expected, while changing ε_η only slightly and making no noticeable difference to the diagnostics presented in Figs. 3 and 4. We are thus confident that the chosen η_4 is appropriate and that ε_η is not adversely affected by grid-scale effects.

Forcing. The plasma is driven at the largest scales in the box with the forcing terms $\mathbf{F}_\perp^U$ and $\mathbf{F}_\perp^B$ in equations (1) and (2), respectively. Given that our elongated box is designed to represent a small patch of a much larger system, these terms are supposed to crudely mimic the effect of the larger-scale turbulence on our box's outer scale. As in ref. [32], we opted to design the forcing to inject energy and cross helicity at a constant rate through time, which necessarily requires $\mathbf{F}_\perp^U$ and $\mathbf{F}_\perp^B$ to be adjusted to respond to the state of the plasma. We thus defined $\mathbf{F}_\perp^U = f^U \mathbf{F}_0$ and $\nabla \times \mathbf{F}_\perp^B = f^B \mathbf{F}_0$, where the forcing function $\mathbf{F}_0$ was divergence-free and purely perpendicular to $\mathbf{B}_0$ (no z component), which implies that the forcing is nearly purely Alfvénic (its compressive part is small). $\mathbf{F}_0$ was evolved through time as an Ornstein–Uhlenbeck process for each mode with $2\pi/L_j \le k_j \le 4\pi/L_j$, where j represents each direction x, y and z (the correlation time is $t_{corr} = \tau_A/2$). At each time step, we computed $n\mathbf{u}_i \cdot \mathbf{F}_\perp^U$ and $\mathbf{B} \cdot (\nabla \times \mathbf{F}_\perp^B)$ and adjusted the values of f^U and f^B to make the injected energy and cross helicity equal to their desired values (ε and ε_H, respectively, with $\varepsilon_H = 0.9\varepsilon$). This process required inverting the curl to compute $\mathbf{F}_\perp^B$, which was carried out using a Fourier transform; by adding the magnetic force in this way and evolving $\mathbf{B}$ using the standard constrained-transport algorithm of PEGASUS++, we ensured that $\nabla \cdot \mathbf{B} = 0$ to machine precision.

This forcing method is an extension (to allow for imbalance) of the default routines implemented in the ATHENA code[58], and has thus been used in a number of previous works (for example, ref. [59]). We tested it by separately measuring the energy and cross-helicity injection, which agree almost perfectly with the input values, and by testing the full energy budget of the simulation (see below). A possible downside of this method is that the forcing normalization, f^U and f^B, can change more rapidly than the spatial form of the force $\mathbf{F}_0$. In the simulation, we saw occasional sudden changes in f^U and f^B that seem to be caused by the plasma flow and magnetic-field perturbations (which dominantly propagate in the $\hat{z}$ direction) moving out of phase with the large-scale spatial structure of the forcing (determined by the slow evolution of $\mathbf{F}_0$). To assess the impact of this effect, we restarted the simulation at $t = 10\tau_A$ with a modified version of the forcing that limited the change in f^U and f^B across a timestep δt to $\exp(\pm\Omega_i \delta t/10)$, where the $\pm$ was decided by whether f^U and f^B were above or below the optimal value that gave the input energy and cross-helicity injection. This reduced the sudden changes (high-frequency power) in f^U and f^B at the cost of causing $\epsilon(t)$ and $\varepsilon_H(t)$ to vary considerably (by around ±40%) in time. However, this change made no noticeable difference to the heating, distribution function and spectra, lending confidence in the robustness of our results. Finally, we have confirmed that the helicity barrier also forms robustly in the reduced model of ref. [32] when the outer scales are forced with white-in-time noise (as opposed to with constant energy and cross-helicity injection). Thus, we do not expect our results to be particularly sensitive to the design of the forcing.

Electric-field noise and numerical cooling. A persistent problem for the particle-in-cell method is the influence of electric field noise, which arises due to random density noise from the finite number of numerical particles. In the full-f hybrid-kinetic method with the PEGASUS++ algorithm, a key impact of this noise is a numerical cooling, which slowly drains thermal energy from the system. This was removed from Fig. 1 for clarity, but can be accurately assessed by computing the thermal energy budget, which is shown in Extended Data Fig. 1. The sum of the various contributions to the total rate of change of energy, shown by the thick black line, would equal zero if energy were conserved, but is instead negative, indicating numerical cooling. This feature—although clearly undesirable—can be avoided only by increasing the number of particles per cell (thus increasing computational cost) or by using more filter passes (thus decreasing the effective dynamic range). Its nearly constant value throughout the simulation (including at very early times $t \lesssim \tau_A$, when the forcing is fully absorbed by large-scale mechanical energy and there is no resistive dissipation) suggests that its properties are mostly separate from the development of turbulent heating in the system, justifying the decision to tolerate its presence and remove it from our energy estimates.

Another effect of the particle noise is its direct influence on the spectra. Noisy fluctuations cause an artificial bump in all quantities near the grid scale, which accounts for some of the small-scale flattening of the electric- and magnetic-field spectra in Fig. 2. This can be quantified by computing spectra from the very early stages of the simulation, before the turbulence has developed, when the small-scale fluctuations are purely a result of particle noise. We compared these to the saturated-turbulence spectra in Extended Data Fig. 2. The general conclusion is that for $k_\perp \rho_i \gtrsim 3$, noise makes a reasonable contribution to the spectra, which are thus uncertain in this range. This effect is more severe in this imbalanced simulation than other previous turbulence simulations with PEGASUS++[19,20] precisely because of the transition range, which makes the sub-ρ_i fluctuations very small in magnitude. Again, it can only be ameliorated by increasing the number of particles per cell, which yields small gains for large computational expense (the noise scales $\propto N_{ppc}^{1/2}$). If one subtracts the noise spectra from the saturated spectra (which is probably a reasonable procedure because the noise power is dominated by modes of high $k_\perp$ and k_z, whereas the majority of high-$k_\perp$ power at saturation resides at lower k_z) our main conclusions still hold, with $\mathcal{E}_\mathbf{B}$ and $\mathcal{E}_\mathbf{E}$ re-flattening at $k_\perp \rho_i \simeq 2$ and an $\sim k_\perp^{-0.8}$ KAW range in $\mathcal{E}_\mathbf{E}$ (not shown).

Finally, we note that a different preliminary simulation with a value of ε three times larger, four filter passes and $N_{ppc} = 128$ reproduced the key early time features discussed above, including a double-kinked electric field spectrum (this simulation was run only until $t \simeq 5\tau_A$, which is before magnetic-field spectrum develops a double kink). In addition to causing the large-scale energy to grow faster in time, the larger ε in this case caused the noise in spectra and the numerical cooling to be proportionally much smaller. We are thus confident that the physical features reported in the main text are robust.

Measurement of the parallel spectrum. In Figs. 2 and 3, we measured parallel spectra using a field-line following method, which we describe here. While structure–function methods are more commonly used to study anisotropic MHD turbulence[37], the extremely steep parallel spectra (up to $\sim k_\parallel^{-6}$) caused by the helicity barrier are not well captured by structure functions[60]. Our field-line-following method computes a $(k_\perp, k_\parallel)$ spectrum by first constructing N_{lines} magnetic field lines by solving $d\mathbf{r}/ds = \hat{b}(\mathbf{r}) = \mathbf{B}/|\mathbf{B}|$ from field line $s = 0$ to $s = L_{lines}$, where the periodicity of the system allows $L_{lines} > L_\parallel$ if desired. The field of interest $X(\mathbf{x})$ (for example, $X = B_y$ or $X = E_z$) is then Fourier-filtered to a given bin in $k_\perp = \sqrt{k_x^2 + k_y^2}$, giving $X_{k_\perp}(\mathbf{x})$, which is then interpolated onto the coordinates $\mathbf{r}(s)$ of the previously computed field lines. The spectrum of $X_{k_\perp}[\mathbf{r}(s)]$ is then computed in the s direction, which becomes a single $k_\perp$ slice of $\mathcal{E}_X(k_\perp, k_\parallel)$. Repeating this process across a grid of $k_\perp$ yields the full 2D spectrum. Note that if this process is applied to compute a $(k_\perp, k_z)$ spectrum (that is, $\mathbf{r}(s)$ in the $\hat{z}$ direction), it yields the same result as computing the spectrum in the standard way with a 3D Fourier transform. Through experimentation, we found that $L_{lines} = 10L_\parallel$ and $N_{lines} = N_x N_y L_\parallel / L_{lines}$ gave high-quality results (although results were almost independent of L_{lines} for $L_{lines} \gtrsim 2L_\parallel$). In addition, a Hamming filter was used to compute the $k_\parallel$ spectra because the s direction was non-periodic. Because the field-perpendicular plane is assumed to be the x, y plane, the method is valid in the 'reduced-MHD' limit of $L_\perp/L_\parallel \approx \delta B_\perp/B_0 \ll 1$. A pure parallel spectrum, as in the inset of Fig. 2, can be computed from $\int dk_\perp \, \mathcal{E}_X(k_\perp, k_\parallel)$, which recovers the standard field-line-parallel spectrum[61].

We compared our method to the more conventional method of computing 2D spectra via structure functions, finding reasonable agreement where both were appropriate. Extended Data Fig. 3 shows $\mathcal{E}_{B\perp}(k_\perp, k_\parallel) = \mathcal{E}_{B_x} + \mathcal{E}_{B_y}$ for the balanced simulation, illustrating how we recovered the previously discussed $k_\parallel \approx k_\perp^{2/3}$ and $k_\parallel \approx k_\perp$ ranges above and below the ion-Larmor scale $k_\perp \rho_i \approx 1$ (ref. [19]). Our method also recovered the expected extremely steep scaling in $k_\parallel$ ($\mathcal{E}_{B\perp} \propto k_\parallel^{-6}$) predicted by theory at low $k_\perp$ (see appendix B of ref. [37]; not shown). A more quantitative comparison revealed that the most notable difference compared with the structure–function method is that the 2D spectrum is shifted upwards (to larger $k_\parallel$); thus, compared with the structure–function method, the field-line-following method generally estimates $k_\parallel(k_\perp)$ to be a factor of ≃2 larger across all $k_\perp$.

Note that the helicity spectrum (Fig. 3c) was computed by binning in $(k_\perp, k_z)$, rather than $(k_\perp, k_\parallel)$, which gave a cleaner spectrum. The difficulty with $(k_\perp, k_\parallel)$ seems to relate to $\mathcal{H}_\mathbf{k}$ explicitly involving $\mathbf{k}$ in its definition[44,62], which may cause problems with the non-orthogonal coordinate system $(k_x, k_y, k_\parallel)$. The $(k_\perp, k_z)$ spectrum of $B_\perp$ looks broadly similar to its $(k_\perp, k_\parallel)$ spectrum, particularly in the $k_z > k_\perp$ region of ICWs, so Fig. 3b,c can be usefully compared on a qualitative level.

Heating through quasilinear diffusion on ICWs. *Computation of the resonance contours for parallel ICWs.* Here we describe in more detail the computation of the quasilinear ICW 'scattering contours' shown in Fig. 4. Quasilinear theory[24] is based on the idea that particles interact strongly with a spectrum of ICWs if they satisfy the cylotron-resonance condition

$$\omega_\mathbf{k} - k_\parallel w_\parallel = \pm\Omega_i. \tag{4}$$

Here $\omega_\mathbf{k}$ is the wave's frequency and $w_\parallel$ is the ion's parallel velocity (both are measured in the fluid frame in which the plasma is stationary); equation (4) expresses the condition for the Doppler-shifted wave frequency to be resonant with the ion's gyromotion, which causes the wave and the particle to interact strongly. In the frame moving with the wave's phase velocity $v_{ph} = \omega_\mathbf{k}/k_\parallel$, the magnetic field perturbation is constant in time. This means that the electric field must be purely potential in this frame ($\mathbf{E} = -\nabla\Phi$), and a particle should approximately conserve its kinetic energy as it scatters from the wave. Thus, if equation (4) has only one solution for each $w_\parallel$—in other words, when there exist only waves of a single $k_\perp$ (for example, if only parallel waves exist) or when $\omega_\mathbf{k}$ is a function of $k_\parallel$ only—particles diffuse only along specific scattering contours in the $w_\perp$–$w_\parallel$ plane. If the waves are non-dispersive (that is, if $\omega_\mathbf{k} \propto k_\parallel$) these are semicircles of constant particle energy in the wave's frame $\epsilon_{K,wave} = (w_\parallel - \omega_\mathbf{k}/k_\parallel)^2 + w_\perp^2$. More generally, the scattering

contours are defined by the null solutions $\eta(w_\perp, w_\parallel) = \text{const.}$ of the quasilinear diffusion operator[24,25,47],

$$\left[1 - \frac{w_\parallel}{v_{\rm ph}(w_\parallel)}\right]\frac{\partial \eta}{\partial w_\perp} + \frac{w_\perp}{v_{\rm ph}(w_\parallel)}\frac{\partial \eta}{\partial w_\parallel} = 0, \tag{5}$$

where $v_{\rm ph}(w_\parallel) = \omega_{\mathbf{k}}/k_\parallel$ for the $w_\parallel$ that satisfies the resonant condition (4). If f_i is a decreasing function along the scattering contours, the quasilinear diffusion heats the plasma in the range of $w_\parallel$ where there is appreciable power in waves of the corresponding resonant $k_\parallel$; if f_i is an increasing function along the scattering contours, the distribution function will become unstable, growing the wave power in the resonant range of $\mathbf{k}$.

To compute the scattering contours, we assumed the cold-plasma ICW dispersion relation for parallel propagating waves ($k_\perp = 0$), which is

$$\omega_{\mathbf{k}} = k_\parallel v_{\rm A}\sqrt{1 - \omega_{\mathbf{k}}/\Omega_{\rm i}} \quad \Rightarrow \quad v_{\rm ph}(k_\parallel) = \frac{v_{\rm A}}{2\Omega_{\rm i}}\left(\sqrt{k_\parallel^2 v_{\rm A}^2 + 4\Omega_{\rm i}^2} - k_\parallel v_{\rm A}\right). \tag{6}$$

A parametric solution for η can be found by solving equations (4) and (6) for $v_{\rm ph}(w_\parallel)$, and then using this in the solution of equation (5), $w_\perp^2 + w_\parallel^2 - 2\int \mathrm{d}w'\, v_{\rm ph}(w') = \text{const.}$ This yields the contours[63]

$$\frac{w_\perp^2}{v_{\rm A}^2} + \frac{1}{y^2} + \ln y - \sinh^{-1}\frac{y}{2} = \text{const.} \tag{7}$$

where $y = k_\parallel v_{\rm A}/\Omega_{\rm i}$ relates to $w_\parallel$ implicitly through equation (4) (the full explicit solution is uninformatively complex).

The quasilinear diffusion process relies on maintaining wave power in the relevant range of $k_\parallel$, but the simulation exhibits a steep drop in the spectrum for $k_\parallel d_i \gtrsim 1$ (Fig. 3). This is probably because linear ICWs become strongly damped at $k_\parallel d_i \simeq 1$ at $\beta_i = 0.3$ (as can be shown by solving the hot-plasma dispersion relation). This implies a minimum $|w_\parallel| = w_{\parallel,d_i}$ above which f_i should tend to flatten along the scattering contours and below which it should not. This is computed from equations (6) and (4) by solving for $w_\parallel$ at $k_\parallel = d_i^{-1}$, giving

$$w_{\parallel,d_i} \approx -\frac{1}{2}\left(3 - \sqrt{5}\right) v_{\rm A}. \tag{8}$$

The contours (7) and the cutoff (8), which are plotted in Fig. 4a, provide an exceptionally good match to the shape of f_i.

Oblique ICWs. The above calculation assumes that only parallel waves exist in the plasma. In the presence of oblique waves, the dependence of $v_{\rm ph}(k_\parallel)$ on $k_\perp$ means that a range of scattering contours exist for a given $w_\parallel$. References[47] and[64] provide a compelling argument as to why it is the parallel ICW scattering contours that should determine the form of f_i, even if oblique modes provide the primary heating power (see also ref. [25]). They note that the dependence of $v_{\rm ph}(k_\parallel)$ on $k_\perp$ is such that higher-$k_\perp$ modes produce scattering contours that are steeper (that is, $(\partial\eta/\partial w_\perp)/(\partial\eta/\partial w_\parallel)$ is larger). A quasilinear diffusion process along these contours will thus produce an f_i that is an increasing function along the resonance contours of parallel modes (equation (5)), which will be unstable and generate parallel ICWs. A spectrum of driven oblique modes will therefore generate parallel ICWs in the process of heating—effectively a kinetic mechanism for spectral transfer from oblique to parallel modes—creating an f_i that is almost flat along the parallel ICW resonance contours.

This phenomenology provides a reasonable explanation for the behaviour that we observed in our simulation: in the saturated stage, a clear population of parallel ($k_\perp \approx 0$) ICWs appeared (Fig. 3b), even though the turbulent cascade of energy to such modes is probably slow compared with the power input into oblique modes (indeed, the power in parallel modes is quite small earlier in the simulation). In addition, a careful examination of Fig. 4a shows that the contours of f_i are very slightly steeper than the parallel ICW scattering contours, which should also be expected from the phenomenology because the shape of f_i results from a balance between heating from oblique modes (which occurs on contours that are considerably steeper than those of f_i) and cooling/instability from parallel modes. (However, we caution that there are also other explanations for the different contours, such as differences between the $\beta_i = 0.3$ and cold-plasma ICW dispersion relations or higher-order resonances.) Such a mechanism also implies that the ICW heating process can continue even after f_i becomes perfectly flat along the parallel ICW resonance contours. This is an important feature of this heating process for application to the solar wind, and seems to be what we observe in the saturated state: after $t \approx 14\tau_{\rm A}$ heating continues but f_i expands outwards across the scattering contours. Potential complications with this scenario arise from higher-order resonances (which are possible with oblique but not with parallel ICWs) and electron damping by ICWs at $k_\parallel d_i \ll 1$ (ref. [65]), but these are generally expected to be unimportant to the overall physics[47].

Finally, we emphasize that by the end of the simulation, the average thermal anisotropy of the full distribution was only $T_\perp/T_\parallel \approx 1.03$. This value was small for two main reasons: first, because $\tau_{\rm heat} \simeq 54\tau_{\rm A}$ was longer than the simulation duration and second, because of the development of the beam, which contributed to the parallel temperature. Given that this $T_\perp/T_\parallel$ was far below the usual bi-Maxwellian ICW instability threshold of $T_\perp/T_\parallel \approx 1.7$ at $\beta \approx 0.3$ that is often used in observational studies[66], it is clear that the detailed shape of the distribution function must be considered to understand its stability to parallel ICWs and other wave modes.

Computation of $D^E_{\perp\perp}$. The perpendicular energy diffusion coefficient provides a useful quantitative diagnostic of the plasma heating mechanism. It is defined by assuming that

$$\frac{\partial f_i}{\partial t} = \frac{\partial}{\partial e_\perp}\left(D^E_{\perp\perp}\frac{\partial f_i}{\partial e_\perp}\right), \tag{9}$$

where $e_\perp = w_\perp^2/2$ is the perpendicular kinetic energy per unit mass. The assumption that the evolution of f_i was described by equation (9), which is simply a diffusion equation in perpendicular energy, hinges on perpendicular heating dominating over parallel heating, as was indeed the case in our simulation (at least in the $w_\parallel \lesssim 0$ part of velocity space). In standard quasilinear theory (ignoring the oblique–parallel mode interaction discussed above), the resonance condition depends only on the parallel velocity and the fluctuation spectrum, implying that the velocity diffusion coefficient is independent of $w_\perp$ and thus that the energy diffusion coefficient scales as $D^E_{\perp\perp} \propto w_\perp^2$. Numerically, we computed $D^E_{\perp\perp}$ directly from equation (9) using

$$D^E_{\perp\perp} = \left(\frac{\partial f_i}{\partial e_\perp}\right)^{-1}\int_0^{e_\perp} \mathrm{d}e'\,\frac{\partial f_i}{\partial t}, \tag{10}$$

with the full expression integrated over a range of $w_\parallel$ (this is method II of ref. [48]). We also compared this result to a direct measurement of the perpendicular heating from $D^E_{\perp\perp} = -(\partial Q_\perp/\partial e_\perp)/(\partial f_i/\partial e_\perp)$, where $\partial Q_\perp/\partial e_\perp$ is a direct measure of the heating of particles by electric fields based on $\partial Q_\perp/\partial w_\perp = e\langle \mathbf{w}_\perp \cdot \mathbf{E}_\perp f_i\rangle$, and $\langle \mathbf{w}_\perp \cdot \mathbf{E}_\perp f_i\rangle$ was computed from ion velocities and electric fields during the simulation. This measurement, although noisier, recovered very similar results to equation (10). Further discussion can be found in ref. [48] and ref. [20], particularly in appendix A of ref. [20].

Stochastic heating. Here we address whether, in addition to quasilinear ICW heating, stochastic ion heating[16] might play an important role in turbulence with a helicity barrier. The mechanism is of particular interest, given its prominence in previous theoretical and observational studies[20,67,68]. Possible scenarios could involve multiple heating mechanisms operating at a particular time, or a transition from one heating mechanism to another as f_i changes shape through time. We found no evidence for such behaviour in this simulation: $D^E_{\perp\perp}$ seemed to maintain its quasilinear scaling $D^E_{\perp\perp} \propto w_\perp^2$ throughout, and f_i did not deviate from the scattering contours as it evolved in the saturated state.

We speculate that in this simulation, the lack of stochastic heating is simply a consequence of its small electric potential (Φ) fluctuations around $k_\perp\rho_i \approx 1$, which were required to make ion gyro-orbits sufficiently random to cause heating[16]. In Extended Data Fig. 4, we compare the spectrum of Φ ($\mathcal{E}_\Phi$) in the imbalanced simulation and the balanced simulation[19]. $\mathcal{E}_\Phi(k_\perp\rho_i = 1)$ grew only modestly during the imbalanced simulation, despite the growth in $\mathcal{E}_\Phi$ at larger scales, because of the steep drop at $k_\perp\rho_i < 1$ due to the helicity barrier. Coupled with its larger box, we see that although the imbalanced simulation saturated with larger amplitude turbulence, its ion-gyroscale Φ fluctuations were smaller than in the balanced run. Given that stochastic heating plays only a modest role in this balanced run (it became subdominant after several turnover times due to flattening of the core of f_i; refs. [19,20]) this difference in Φ may be sufficient to render stochastic heating unimportant in imbalanced turbulence at these parameters.

It is unclear whether stochastic heating would play a role in other regimes or over longer timescales. Provided gyroscale fluctuations have sufficient amplitudes, stochastic heating is expected to be more robust at lower β because more heating occurs before it is quenched by the flattening of the core of f_i (ref. [16]). This conclusion is supported by the $\beta \approx 1/9$ hybrid simulation of ref. [20]. On the other hand, test-particle simulations show a strong reduction in the efficiency of heating of $w \approx v_{\rm A}$ ($\beta \approx 1$) particles in imbalanced, compared with balanced, turbulence[21]. If a similar reduction occurs also in the $w \ll v_{\rm A}$, low-β regime, the effectiveness of stochastic heating in turbulence with a helicity barrier may also be limited. Further work is needed. However, it is worth noting that even if stochastic heating, rather than ICW heating, eventually absorbs the turbulent energy flux, the helicity barrier could remain a key ingredient in solar-wind heating. Just as for ICW heating, the barrier would allow turbulent fluctuations to grow in amplitude sufficiently to enable ion heating, rather than fluctuations dissipating their energy into electron heating if their amplitude is initially too small.

Landau damping and the ion beam. An interesting feature of the ion distribution function shown in Fig. 4 is the plateau $w_\perp \approx 0$, $w_\parallel \approx v_{\rm A}$. This forms a modestly super-Alfvénic beam with similar properties[2,49] and directionality[69] to those observed in the solar wind. Here we present evidence that this feature is a result of

Landau damping of perpendicular Alfvén waves as they become dispersive (speed up) near $k_\perp \rho_i \approx 1$. Test-particle calculations have shown this process to be highly effective[51].

Extended Data Fig. 5 compares the measured parallel heating of the distribution function

$$\left\langle \frac{\partial e_\parallel f_i}{\partial t} \right\rangle (w_\parallel) = \int \mathrm{d}e_\perp \, \frac{1}{2} w_\parallel^2 \, \frac{\partial f_i}{\partial t}, \tag{11}$$

to the parallel heating inferred from the work done by the parallel electric field $e\langle w_\parallel E_\parallel f_i \rangle$, which is computed during the simulation from particle trajectories. We see a clear peak in both quantities at $w_\parallel \approx v_A$. As discussed above (equation (10)), both methods measure plasma heating but they can differ by a total derivative. Their similarity in Extended Data Fig. 5—particularly the similarity in their magnitudes even at different times during the simulation when $\langle \partial(e_\parallel f_i)/\partial t \rangle$ differs—suggests that parallel electric field work (that is, Landau damping) is responsible for the formation of the beam.

Data availability

The 6D simulations presented in this article generated approximately 30 TB of data. Interested parties are invited to contact the corresponding author to make arrangements for the transfer of those data.

Code availability

All analysis scripts presented in this work are available on request from the corresponding author. The PEGASUS++ code will be made publicly available in the near future in conjunction with a detailed publication about its numerical methods. Readers can contact the corresponding author to get updates.

Received: 9 September 2021; Accepted: 1 February 2022;
Published online: 24 March 2022

References

1. Cranmer, S. R. & Winebarger, A. R. The properties of the solar corona and its connection to the solar wind. *Ann. Rev. Astron. Astrophys.* **57**, 157–187 (2019).
2. Marsch, E. Kinetic physics of the solar corona and solar wind. *Living Rev. Solar Phys.* **3**, 1 (2006).
3. Parker, E. N. Dynamical theory of the solar wind. *Space Sci. Rev.* **4**, 666–708 (1965).
4. Hansteen, V. H. & Leer, E. Coronal heating, densities, and temperatures and solar wind acceleration. *J. Geophys. Res.* **100**, 21577–21594 (1995).
5. Kohl, J. L. et al. First results from the SOHO Ultraviolet Coronagraph Spectrometer. *Sol. Phys.* **175**, 613–644 (1997).
6. Cranmer, S. R., Field, G. B. & Kohl, J. L. Spectroscopic constraints on models of ion cyclotron resonance heating in the polar solar corona and high-speed solar wind. *Astrophys. J.* **518**, 937–947 (1999).
7. Bale, S. D. et al. Highly structured slow solar wind emerging from an equatorial coronal hole. *Nature* **576**, 237–242 (2019).
8. De Pontieu, B. et al. Chromospheric Alfvénic waves strong enough to power the solar wind. *Science* **318**, 1574–1577 (2007).
9. Tomczyk, S. et al. Alfvén waves in the solar corona. *Science* **317**, 1192–1196 (2007).
10. Velli, M., Grappin, R. & Mangeney, A. Turbulent cascade of incompressible unidirectional Alfvén waves in the interplanetary medium. *Phys. Rev. Lett.* **63**, 1807–1810 (1989).
11. van Ballegooijen, A. A., Asgari-Targhi, M., Cranmer, S. R. & DeLuca, E. E. Heating of the solar chromosphere and corona by Alfvén wave turbulence. *Astrophys. J.* **736**, 3 (2011).
12. Shoda, M., Suzuki, T. K., Asgari-Targhi, M. & Yokoyama, T. Three-dimensional simulation of the fast solar wind driven by compressible magnetohydrodynamic turbulence. *Astrophys. J. Lett.* **880**, L2 (2019).
13. Quataert, E. & Gruzinov, A. Turbulence and particle heating in advection-dominated accretion flows. *Astrophys. J.* **520**, 248–255 (1999).
14. Schekochihin, A. A., Kawazura, Y. & Barnes, M. A. Constraints on ion versus electron heating by plasma turbulence at low beta. *J. Plasma Phys.* **85**, 905850303 (2019).
15. Schekochihin, A. A. et al. Astrophysical gyrokinetics: kinetic and fluid turbulent cascades in magnetized weakly collisional plasmas. *Astrophys. J. Suppl. Ser.* **182**, 310 (2009).
16. Chandran, B. D. G. et al. Perpendicular ion heating by low-frequency Alfvén-wave turbulence in the solar wind. *Astrophys. J.* **720**, 503–515 (2010).
17. Chandran, B. D. G., Dennis, T. J., Quataert, E. & Bale, S. D. Incorporating kinetic physics into a two-fluid solar-wind model with temperature anisotropy and low-frequency Alfvén-wave turbulence. *Astrophys. J.* **743**, 197 (2011).
18. Vech, D., Klein, K. G. & Kasper, J. C. Nature of stochastic ion heating in the solar wind: testing the dependence on plasma beta and turbulence amplitude. *Astrophys. J. Lett.* **850**, L11 (2017).
19. Arzamasskiy, L., Kunz, M. W., Chandran, B. D. G. & Quataert, E. Hybrid-kinetic simulations of ion heating in Alfvénic turbulence. *Astrophys. J.* **879**, 53 (2019).
20. Cerri, S. S., Arzamasskiy, L. & Kunz, M. W. On stochastic heating and its phase-space signatures in low-beta kinetic turbulence. *Astrophys. J.* **916**, 120 (2021).
21. Teaca, B., Weidl, M. S., Jenko, F. & Schlickeiser, R. Acceleration of particles in imbalanced magnetohydrodynamic turbulence. *Phys. Rev. E* **90**, 021101 (2014).
22. Isenberg, P. A. & Vasquez, B. J. Perpendicular ion heating by cyclotron resonant dissipation of turbulently generated kinetic Alfvén waves in the solar wind. *Astrophys. J.* **887**, 63 (2019).
23. Hollweg, J. V. & Isenberg, P. A. Generation of the fast solar wind: a review with emphasis on the resonant cyclotron interaction. *J. Geophys. Res. Space Phys.* **107**, SSH 12-1–SSH 12-37 (2002).
24. Kennel, C. F. & Engelmann, F. Velocity space diffusion from weak plasma turbulence in a magnetic field. *Phys. Fluids* **9**, 2377–2388 (1966).
25. Isenberg, P. A. & Vasquez, B. J. A kinetic model of solar wind generation by oblique ion-cyclotron waves. *Astrophys. J.* **731**, 88 (2011).
26. Kasper, J. C., Maruca, B. A., Stevens, M. L. & Zaslavsky, A. Sensitive test for ion-cyclotron resonant heating in the solar wind. *Phys. Rev. Lett.* **110**, 091102 (2013).
27. Zhao, G. Q. et al. Dependence of ion temperatures on alpha-proton differential flow vector and heating mechanisms in the solar wind. *Astrophys. J. Lett.* **889**, L14 (2020).
28. Hollweg, J. V. Compressibility of ion cyclotron and whistler waves: can radio measurements detect high-frequency waves of solar origin in the corona? *J. Geophys. Res.* **105**, 7573–7582 (2000).
29. Shebalin, J. V., Matthaeus, W. H. & Montgomery, D. Anisotropy in MHD turbulence due to a mean magnetic field. *J. Plasma Phys.* **29**, 525–547 (1983).
30. Woodham, L. D. et al. Parallel-propagating fluctuations at proton-kinetic scales in the solar wind are dominated by kinetic instabilities. *Astrophys. J. Lett.* **884**, L53 (2019).
31. Voitenko, Y. & Goossens, M. Excitation of high-frequency Alfvén waves by plasma outflows from coronal reconnection events. *Sol. Phys.* **206**, 285–313 (2002).
32. Meyrand, R., Squire, J., Schekochihin, A. A. & Dorland, W. On the violation of the zeroth law of turbulence in space plasmas. *J. Plasma Phys.* **87**, 535870301 (2021).
33. Cho, J. Magnetic helicity conservation and inverse energy cascade in electron magnetohydrodynamic wave packets. *Phys. Rev. Lett.* **106**, 191104 (2011).
34. Kunz, M. W., Stone, J. M. & Bai, X.-N. Pegasus: a new hybrid-kinetic particle-in-cell code for astrophysical plasma dynamics. *J. Comp. Phys.* **259**, 154–174 (2014).
35. Chen, C. H. K. Recent progress in astrophysical plasma turbulence from solar wind observations. *J. Plasma Phys.* **82**, 535820602 (2016).
36. Davidson, P. A. *Turbulence: An Introduction for Scientists and Engineers* (Oxford Univ. Press, 2004).
37. Schekochihin, A. A. MHD turbulence: a biased review. Preprint at https://arxiv.org/abs/2010.00699 (2021).
38. McManus, M. D. et al. Cross helicity reversals in magnetic switchbacks. *Astrophys. J. Suppl. Ser.* **246**, 67 (2020).
39. Leamon, R. J. et al. Observational constraints on the dynamics of the interplanetary magnetic field dissipation range. *J. Geophys. Res.* **103**, 4775–4788 (1998).
40. Bowen, T. A. et al. Constraining ion-scale heating and spectral energy transfer in observations of plasma turbulence. *Phys. Rev. Lett.* **125**, 025102 (2020).
41. Chen, C. H. K., Boldyrev, S., Xia, Q. & Perez, J. C. Nature of subproton scale turbulence in the solar wind. *Phys. Rev. Lett.* **110**, 225002 (2013).
42. Duan, D. et al. Anisotropy of solar wind turbulence in the inner heliosphere at kinetic scales: PSP observations. *Astrophys. J. Lett.* **915**, L8 (2021).
43. Huang, S. Y. et al. The ion transition range of solar wind turbulence in the inner heliosphere: Parker Solar Probe observations. *Astrophys. J. Lett.* **909**, L7 (2021).
44. Howes, G. G. & Quataert, E. On the interpretation of magnetic helicity signatures in the dissipation range of solar wind turbulence. *Astrophys. J. Lett.* **709**, L49–L52 (2010).
45. Huang, S. Y. et al. Kinetic scale slow solar wind turbulence in the inner heliosphere: coexistence of kinetic Alfvén Waves and Alfvén ion cyclotron waves. *Astrophys. J. Lett.* **897**, L3 (2020).
46. Zhao, G. Q. et al. Magnetic helicity signature and its role in regulating magnetic energy spectra and proton temperatures in the solar wind. *Astrophys. J.* **906**, 123 (2021).
47. Chandran, B. D. G. et al. Resonant interactions between protons and oblique Alfvén/ion-cyclotron waves in the solar corona and solar flares. *Astrophys. J.* **722**, 710–720 (2010).
48. Vasquez, B. J., Isenberg, P. A. & Markovskii, S. A. Proton perpendicular heating in turbulence simulations: determination of the velocity diffusion coefficient. *Astrophys. J.* **893**, 71 (2020).

49. Marsch, E. et al. Solar wind protons: three-dimensional velocity distributions and derived plasma parameters measured between 0.3 and 1 AU. *J. Geophys. Res.* **87**, 52–72 (1982).
50. Verniero, J. L. et al. Parker Solar Probe observations of proton beams simultaneous with ion-scale waves. *Astrophys. J. Suppl. Ser.* **248**, 5 (2020).
51. Li, X. et al. A kinetic Alfvén wave and the proton distribution function in the fast solar wind. *Astrophys. J. Lett.* **719**, L190–L193 (2010).
52. Wang, Y. M. & Sheeley, N. R. Solar wind speed and coronal flux-tube expansion. *Astrophys. J.* **355**, 726 (1990).
53. Cranmer, S. R. in *Solar Wind 11/SOHO 16: Connecting Sun and Heliosphere* Special Publication 592 (eds Fleck, B. et al.) 159 (ESA, 2005).
54. Chandran, B. D. G. An approximate analytic solution to the coupled problems of coronal heating and solar-wind acceleration. *J. Plasma Phys.* **87**, 905870304 (2021).
55. Byers, J. A., Cohen, B. I., Condit, W. C. & Hanson, J. D. Hybrid simulations of quasineutral phenomena in magnetized plasma. *J. Comp. Phys.* **27**, 363–396 (1978).
56. Goldreich, P. & Sridhar, S. Toward a theory of interstellar turbulence. Strong Alfvénic turbulence. *Astrophys. J.* **438**, 763–775 (1995).
57. Kasper, J. C. et al. Alfvénic velocity spikes and rotational flows in the near-Sun solar wind. *Nature* **576**, 228–231 (2019).
58. Stone, J. M. et al. Athena: a new code for astrophysical MHD. *Astrophys. J. Suppl. Ser.* **178**, 137–177 (2008).
59. Lynn, J. W., Parrish, I. J., Quataert, E. & Chandran, B. D. G. Resonance broadening and heating of charged particles in magnetohydrodynamic turbulence. *Astrophys. J.* **758**, 78 (2012).
60. Cho, J. & Lazarian, A. Simulations of electron magnetohydrodynamic turbulence. *Astrophys. J.* **701**, 236–252 (2009).
61. Meyrand, R., Kanekar, A., Dorland, W. & Schekochihin, A. A. Fluidization of collisionless plasma turbulence. *Proc. Natl. Acad. Sci. USA* **116**, 1185–1194 (2019).
62. Matthaeus, W. H. & Goldstein, M. L. Measurement of the rugged invariants of magnetohydrodynamic turbulence in the solar wind. *J. Geophys. Res.* **87**, 6011–6028 (1982).
63. Isenberg, P. A. & Lee, M. A. A dispersive analysis of bispherical pickup ion distributions. *J. Geophys. Res.* **101**, 11055–11066 (1996).
64. Pongkitiwanichakul, P., Chandran, B. D. G., Isenberg, P. A. & Vasquez, B. J. Resonant interactions between protons and oblique Alfvén/ion-cyclotron waves. In *Twelfth International Solar Wind Conference* AIP Conference Series Vol. 1216 (eds Maksimovic, M. et al.) 72–75 (AIP, 2010).
65. Gary, S. P. & Borovsky, J. E. Alfvén-cyclotron fluctuations: linear Vlasov theory. *J. Geophys. Res. Space Phys.* **109**, A06105 (2004).
66. Hellinger, P., Trávníček, P., Kasper, J. C. & Lazarus, A. J. Solar wind proton temperature anisotropy: linear theory and WIND/SWE observations. *Geophys. Res. Lett.* **33**, L09101 (2006).
67. Klein, K. G. & Chandran, B. D. G. Evolution of the proton velocity distribution due to stochastic heating in the near-Sun solar wind. *Astrophys. J.* **820**, 47 (2016).
68. Martinović, M. M. et al. The enhancement of proton stochastic heating in the near-Sun solar wind. *Astrophys. J. Suppl. Ser.* **246**, 30 (2020).
69. He, J. et al. Sunward propagating Alfvén waves in association with sunward drifting proton beams in the solar wind. *Astrophys. J.* **805**, 176 (2015).

Acknowledgements

We thank B. Dorland, B. Chandran and A. Mallet for illuminating discussions. J.S. and R.M acknowledge support from the Royal Society Te Apārangi, New Zealand, through Marsden Fund grant number UOO1727 and Rutherford Discovery Fellowship RDF-U001804. M.W.K. and E.Q. were supported by the Department of Energy through the NSF/DOE Partnership in Basic Plasma Science and Engineering, award numbers DE-SC0019046 and DE-SC0019047, with additional support for E.Q. from a Simons Investigator Award from the Simons Foundation. L.A. acknowledges the support of the Institute for Advanced Study, and the work of A.A.S. was supported in part by UK EPSRC grant number EP/R034737/1. This research was part of the Frontera computing project at the Texas Advanced Computing Center, which is made possible by National Science Foundation award number OAC-1818253. Further computational support was provided by the New Zealand eScience Infrastructure (NeSI) high-performance computing facilities, funded jointly by NeSI's collaborator institutions and the NZ MBIE, and through the PICSciE-OIT TIGRESS High Performance Computing Center and Visualization Laboratory at Princeton University. The funders had no role in study design, data collection and analysis, decision to publish or preparation of the manuscript.

Author contributions

J.S. and R.M. conceived the study. L.A., M.W.K. and J.S. developed the numerical methods and model, with J.S. and L.A. performing the simulations. Data analysis and visualization was carried out by J.S. and L.A., with all authors contributing to general understanding and interpretation of the results. The manuscript was written primarily by J.S. with M.W.K, A.A.S. and E.Q. leading revisions and editing.

Competing interests

The authors declare no competing interests.

Additional information

Extended data is available for this paper at https://doi.org/10.1038/s41550-022-01624-z.

Supplementary information The online version contains supplementary material available at https://doi.org/10.1038/s41550-022-01624-z.

Correspondence and requests for materials should be addressed to Jonathan Squire.

Peer review information *Nature Astronomy* thanks Munehito Shoda, Christopher Chen and Philip Isenberg for their contribution to the peer review of this work.

Reprints and permissions information is available at www.nature.com/reprints.

Publisher's note Springer Nature remains neutral with regard to jurisdictional claims in published maps and institutional affiliations.

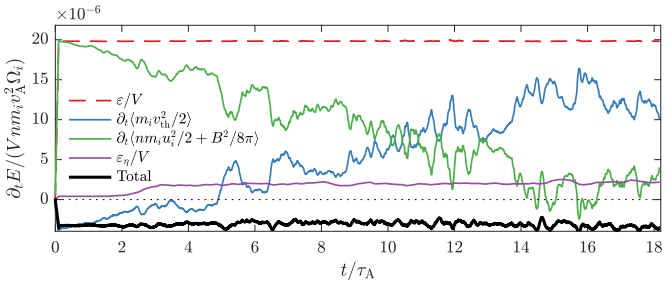

Extended Data Fig. 1 | Electric field noise and numerical cooling. Contributions to the energy budget per unit volume of the imbalanced simulation from the energy injection (ε/V; dashed red line), increase in thermal energy $Q_i = \partial_t \langle m_i v_{\rm th}^2/2\rangle$ (blue line), growth rate of mechanical energy $\partial_t \langle n m_i u_i^2/2 + B^2/8\pi\rangle$ (green line), and resistive dissipation ε_η/V (V is the volume and $\langle \dots \rangle$ denotes a box average). The black line shows the total energy budget Total $= \varepsilon/V - \varepsilon_\eta/V - \partial_t \langle m_i v_{\rm th}^2/2\rangle - \partial_t \langle n m_i u_i^2/2 + B^2/8\pi\rangle$, which is constant and negative, indicating numerical cooling that is effectively independent of the turbulence or the heating of ions.

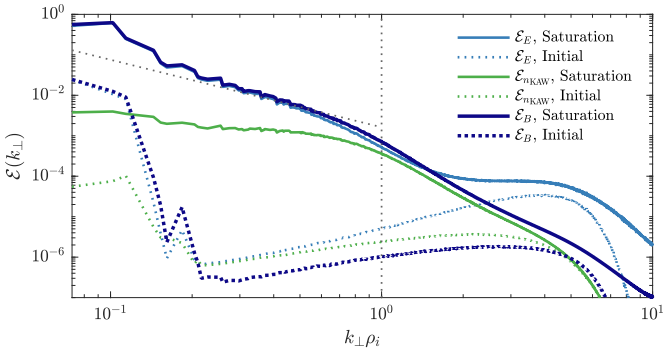

Extended Data Fig. 2 | The effect of particle noise on turbulence spectra. Perpendicular ($k_\perp$) spectra of the magnetic field ($\mathcal{E}_{\boldsymbol{B}}$), electric field $\mathcal{E}_{\boldsymbol{E}}$, and KAW-normalized density $\mathcal{E}_{n_{\mathrm{KAW}}} = \beta_i(1+2\beta_i)\mathcal{E}_n$ in the saturated state (solid lines) and at very early times (averaged over $t \leq 0.2\tau_{\mathrm{A}}$). The latter is from before the turbulence has developed and is thus a proxy for the noise floor in a given quantity. At the smallest scales, $k_\perp\rho_i \gtrsim 3$, spectra are only modestly above the noise floor and therefore uncertain.

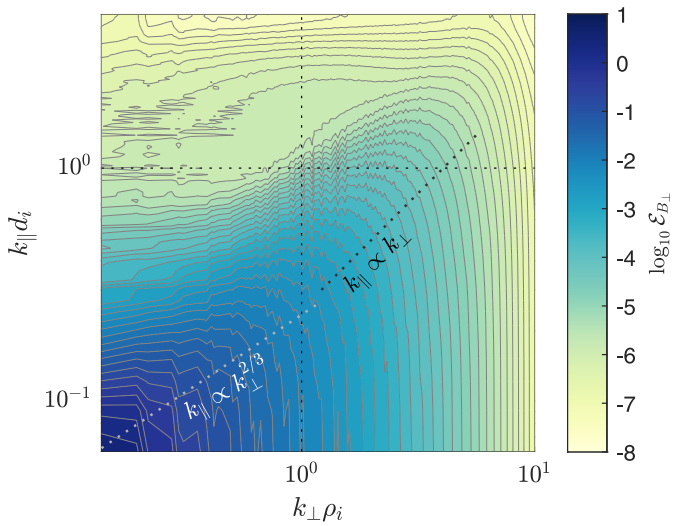

Extended Data Fig. 3 | Measurement of the parallel spectrum. Two-dimensional perpendicular magnetic-field spectrum $\mathcal{E}_{B_\perp}(k_\perp, k_\parallel) = \mathcal{E}_{B_x}(k_\perp, k_\parallel) + \mathcal{E}_{B_y}(k_\perp, k_\parallel)$ from the balanced simulation. The method recovers the large- and small-scale scalings of $k_\parallel$ with $k_\perp$ measured using structure functions (see fig. 2 of ref. [19]), as well as the predicted 2D spectrum in the $k_\perp \rho_i < 1$ range (see appendix B of ref. [37]).

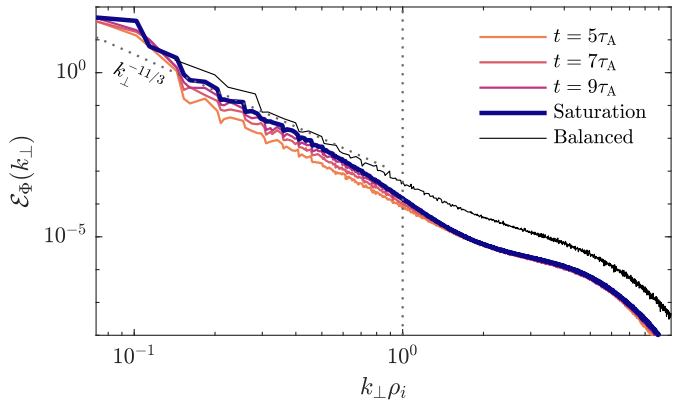

Extended Data Fig. 4 | Assessment of the influence of stochastic heating. We show perpendicular spectra of the electric potential Φ, computed from the curl free part of $\boldsymbol{E}$. Colored lines show various times from the imbalanced simulation. The black line shows the equivalent balanced simulation, which is averaged over the early period of the simulation (between $t = 3.5\tau_A$ and $t = 4.5\tau_A$) when stochastic-ion heating absorbs the majority of the turbulent energy flux[19] Despite the larger turbulence amplitude in the imbalanced simulation, the electric-potential fluctuations around $k_\perp\rho_i \sim 1$ – those important for stochastic heating – are smaller.

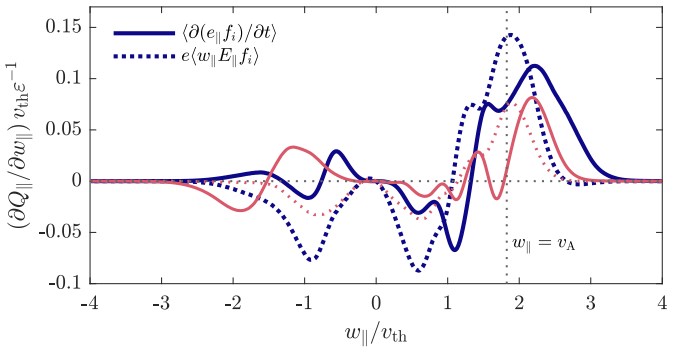

Extended Data Fig. 5 | Development of the ion beam. We compare the rate of change parallel thermal energy (solid lines; see text) with the work done on particles by the parallel electric field $e\langle w_\parallel E_\parallel f_i \rangle$ (dotted lines). The thick dark-blue lines show the saturated state and the orange-pink lines show $t = 7\tau_A$. The similarity of the magnitude and general shape of the two measures of heating suggests that Landau damping is responsible for the formation of the ion beam.